Electronic Supplementary Material (ESI) for Reaction Chemistry & Engineering.

SUPPLEMENTARY INFORMATION

Quantification of Extracrystalline Acid Sites in MFI Zeolites after Post-Synthetic Passivation Treatments using Mesitylene Benzylation Kinetics

Sopuruchukwu Ezenwa, Geoffrey M. Hopping, Eric D. Sauer, Teah Scott, Savanna Mack, Rajamani Gounder*

Davidson School of Chemical Engineering, Purdue University, West Lafayette, IN, 47907, USA

*Corresponding author. E-mail: rgounder@purdue.edu

Table of Contents

Sections

Section S1. Some Reported Ranges of Quantification of External H^+ Content in MFI Zeolites using Probe Molecule Spectroscopy

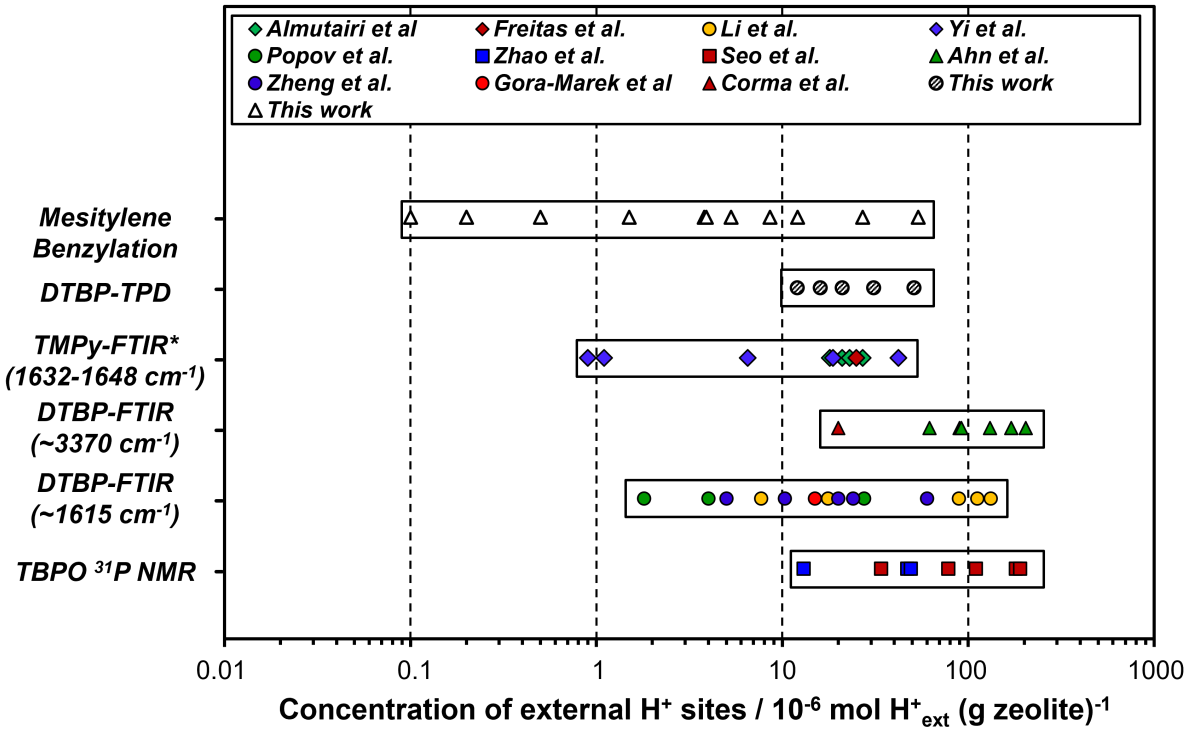

Scheme S1. Some reported ranges[1–11] of external H^+ content (per g zeolite) quantified using probe molecule IR or NMR spectroscopy. Rectangular boxes are added around reported ranges to emphasize the typically encountered equipment detection limits for external H^+ sites in MFI. (*2,4,6-trimethylpyridine (TMPy)–FTIR includes contributions from external Lewis acid sites). The ranges of external H^+ content quantified in this work through DTBP-TPD and mesitylene benzylation with DBE are also included for comparison.

TMPy = 2,4,6-trimethylpyridine (or 2,4,6-collidine)

DTBP = 2,6-di-*tert*-butylpyridine

TBPO = tributylphosphine oxide

Section S2. Elemental and Proton Content for MFI Normalized by Sample Mass

Table S1. Site characterization of MFI samples used in this study (normalized by sample mass)

Sample[a]	Si/Al_{tot}[b]	Elemental content per gram zeolite			
		Si_{total}[b] / 10^{-3} mol Si g^{-1}	Al_{total}[b] / 10^{-3} mol Al g^{-1}	H^+_{total}[c] / 10^{-3} mol NH_3 g^{-1}	H^+_{ext}[d] / 10^{-3} mol DTBP g^{-1}
MFI-13-P	12.5 (±0.5)[e]	15.7 (±0.04)[e]	1.25 (±0.04)[e]	0.93 (±0.05)[e]	0.012
MFI-13-4h-1	12.8	16.0	1.24	0.63	-
MFI-13-48h-1	12.5	15.3	1.22	0.64	-
MFI-13-4h-2	13.3	16.0	1.21	0.74	-
MFI-13-48h-2	13.4	14.4	1.08	0.76	-
MFI-13-4h-2-c1	13.2	16.1	1.21	0.86	-
MFI-13-4h-2-c2	13.5	16.7	1.24	-	-
MFI-13-4h-2-c3	14.2	15.6	1.10	0.71	<0.001
MFI-16-P	15.7	14.5	0.93	0.43	0.021
MFI-16-4h-2-c1	22.5	15.5	0.69	0.42	-
MFI-16-4h-2-c2	24.7	15.2	0.62	-	-
MFI-16-4h-2-c3	26.5	14.3	0.54	0.42	-
MFI-40-P	39.8	15.1	0.38	0.28	0.016
MFI-40-4h-2-c1	41.0	14.0	0.34	0.27	-
MFI-40-4h-2-c2	41.9	15.5	0.37	-	-
MFI-40-4h-2-c3	42.8	15.3	0.36	0.28	-
MFI-C666	46.6	16.8	0.36	0.27	0.031
MFI-C868	47.8	16.5	0.34	0.25	0.051

[a]Parent MFI samples are denoted as MFI-*Si/Al*-P while AHFS-treated MFI samples are denoted as MFI-*Si/Al-duration-concentration-cycle#* where *Si/Al* is the Si/Al ratio of the parent MFI sample, *duration* is the duration of AHFS treatment (4h or 48h), *concentration* is the $Si_{AHFS}/Al_{Zeolite}$ molar ratio (1 or 2), and *cycle#* is the number of successive treatment cycles (c1, c2, c3; omitted for samples with only one treatment cycle).
[b]Determined from ICP-OES of NH_4-form MFI samples . Uncertainties are ±10%, unless otherwise noted.
[c]Determined from NH_3 desorbed during TPD of NH_4-form MFI samples. Uncertainties are ±15%.
[d]Determined from DTBP desorbed during TPD following DTBP adsorption and flushing. Uncertainties are ±15%.
[e]Values in parenthesis reflect the standard deviation of the average of 3–4 replicate measurements.
"-" indicates not measured.

Section S3. XRD Patterns of MFI Samples

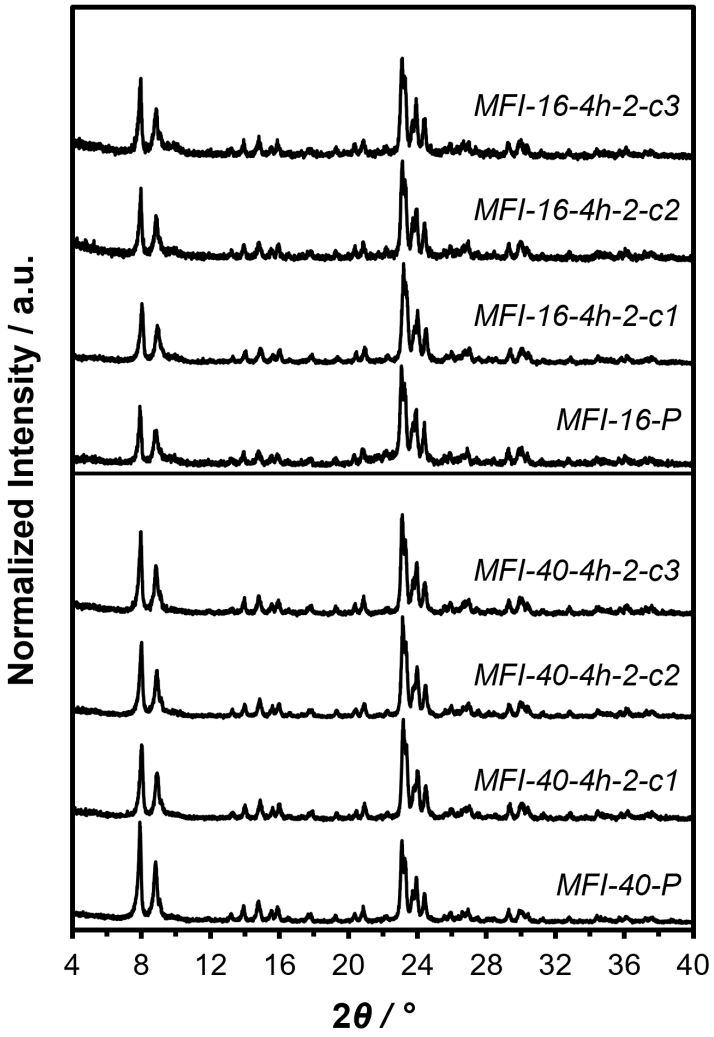

Figure S1. Powder XRD patterns of untreated MFI samples (MFI-16-P, MFI-40-P) and AHFS-treated samples (*MFI-Si/Al-duration-concentration-cycle#*).

Section S4. N_2 Adsorption-Desorption Isotherms of MFI Samples

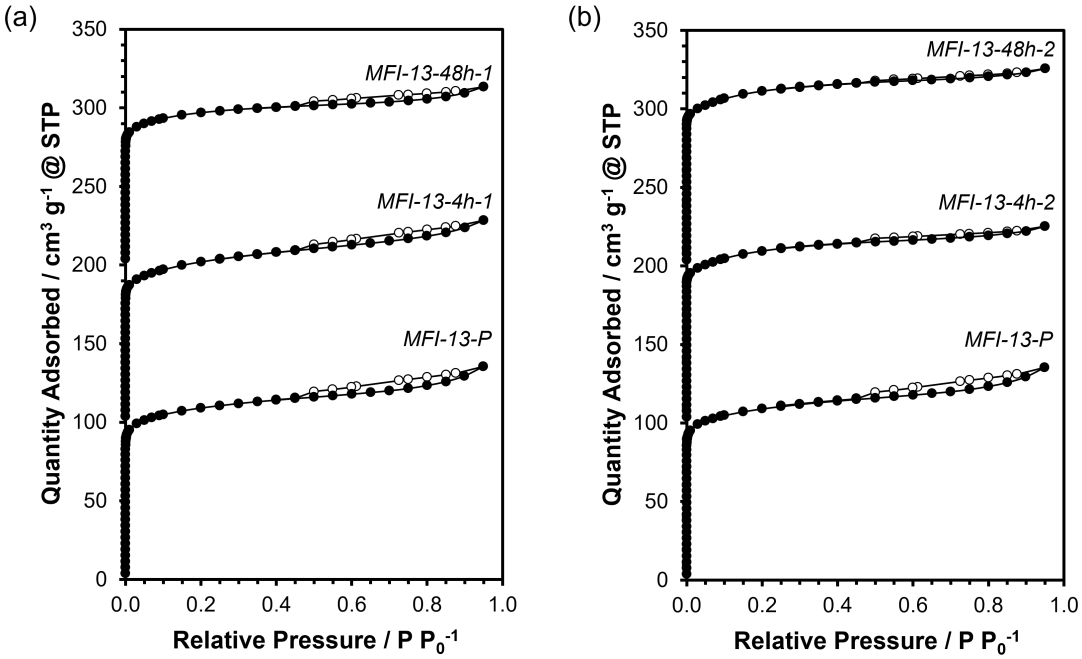

Figure S2 N_2 adsorption (closed)–desorption (open) isotherms (77 K) of parent (MFI-13-P) and AHFS-treated MFI-13 (*MFI-Si/Al-duration-concentration*). The isotherms were vertically offset by 100 cm^3 g^{-1} for clarity.

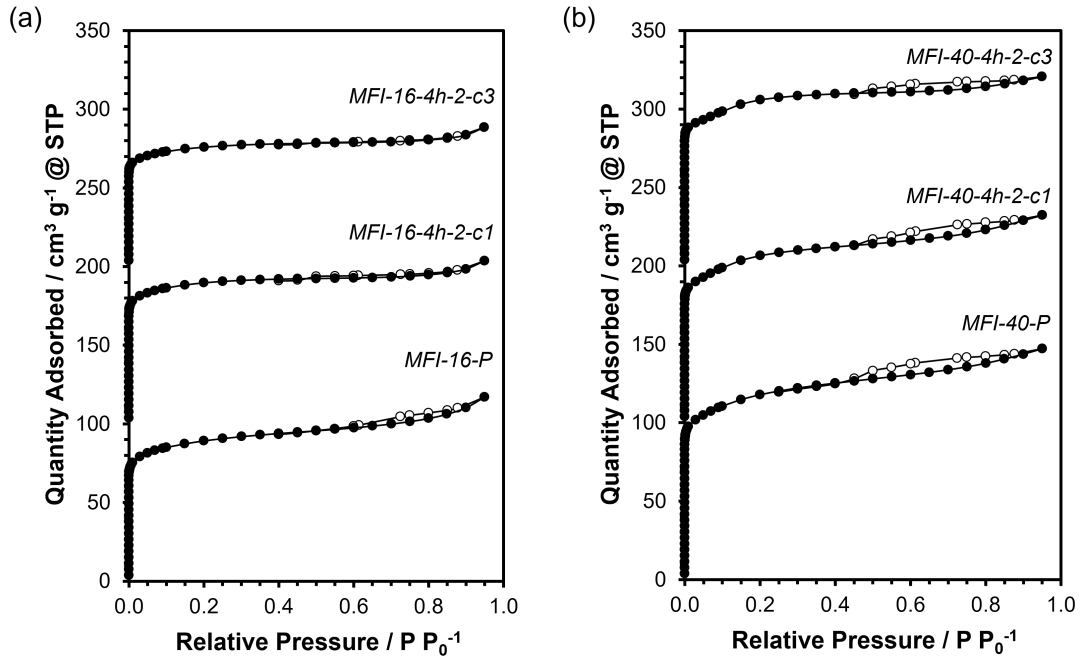

Figure S3. N_2 adsorption (closed)–desorption (open) isotherms (77 K) of parent (MFI-*Si/Al*-P) and AHFS-treated MFI (*MFI-Si/Al-duration-concentration-cycle#*) for (a) MFI-16 and (b) MFI-40 sample series. The isotherms were vertically offset by 100 cm^3 g^{-1} for clarity.

Table S2. Comparison of micropore volume estimation methods.

Micropore volumes were estimated using either the analysis of the semilogarithmic derivative plot of the isotherm $\partial(V_{ads})/\partial(\ln(P/P_0))$ vs $\ln(P/P_0)$, where the first maximum represents the micropore filling transition and the subsequent minimum represents the end of micropore filling (Method 1)[12] or the extrapolation of the linear volumetric N_2 uptake (0.05–0.35 P/P_o) to zero pressure (Method 2). Both methods agreed within ±15%. In the main text, Method 1 was used to compare the micropore volumes and mesopore volumes (difference in total pore volumes measured at $P/P_0 = 0.95$ and micropore volumes)[13] of the parent and AHFS-treated MFI zeolites.

Sample[a]	V_{micro}[a] (Method 1) / $cm^3\ g^{-1}$	V_{micro}[b] (Method 2) / $cm^3\ g^{-1}$
MFI-13-P	0.14 (±0.01)[i]	0.15 (±0.01)[i]
MFI-13-4h-1	0.13	0.14
MFI-13-48h-1	0.13	0.14
MFI-13-4h-2	0.14	0.16
MFI-13-48h-2	0.14	0.16
MFI-13-4h-2-c1	0.13	0.14
MFI-13-4h-2-c2	-	-
MFI-13-4h-2-c3	0.12	0.13
MFI-16-P	0.11	0.13
MFI-16-4h-2-c1	0.12	0.13
MFI-16-4h-2-c2	-	-
MFI-16-4h-2-c3	0.10	0.11
MFI-40-P	0.14	0.16
MFI-40-4h-2-c1	0.13	0.14
MFI-40-4h-2-c2	-	-
MFI-40-4h-2-c3	0.14	0.15
MFI-C666[j]	0.15	0.17
MFI-C868[j]	-	-

[a]Micropore volumes (V_{micro}) estimated from the analysis of the semilogarithmic derivative plot of the isotherm $\partial(V_{ads})/\partial(\ln(P/P_0))$ vs $\ln(P/P_0)$, where the first maximum represents the micropore filling transition and the subsequent minimum represents the end of micropore filling.
[b]Micropore volumes (V_{micro}) estimated using the extrapolation of the linear volumetric N_2 uptake (0.05–0.35 P/P_o) to zero pressure.
"-" indicates not measured.

Section S5. NH_3 TPD Profiles of NH_4-form MFI Samples

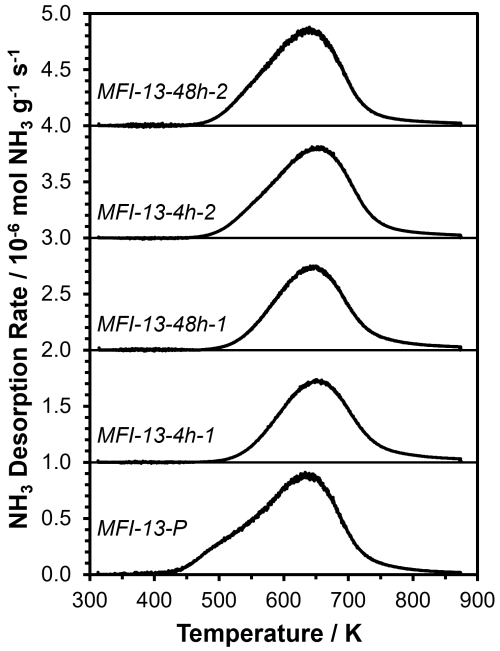

Figure S4. NH_3 TPD profiles on NH_4-form MFI-13-P, MFI-13-4h-1, MFI-13-48h-1, MFI-13-4h-2 and MFI-13-48h-2 samples. TPD profiles are vertically offset for clarity.

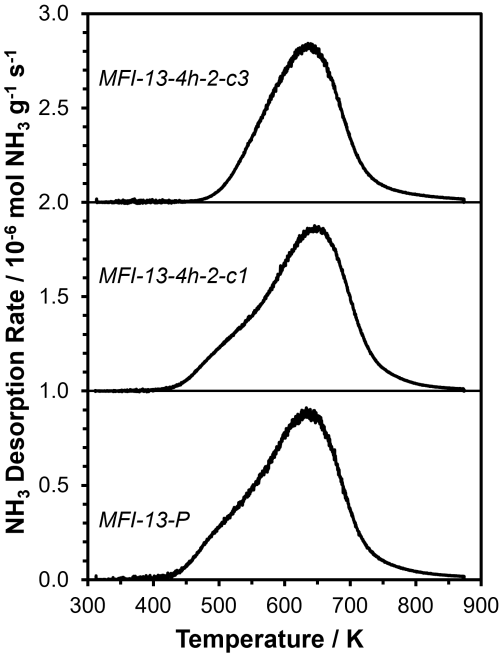

Figure S5. NH_3 TPD profiles on NH_4-form MFI-13-P, MFI-13-4h-2-c1 and MFI-13-4h-2-c3 samples. TPD profiles are vertically offset for clarity.

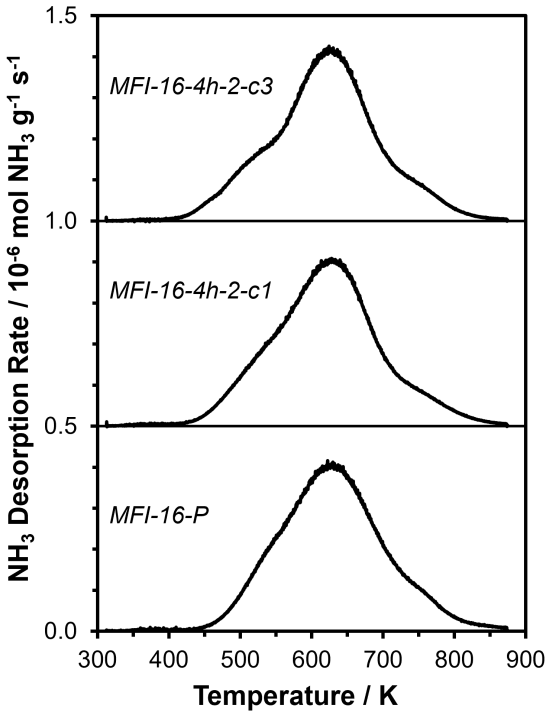

Figure S6. NH_3 TPD profiles on NH_4-form MFI-16-P, MFI-16-4h-2-c1 and MFI-16-4h-2-c3 samples. TPD profiles are vertically offset for clarity.

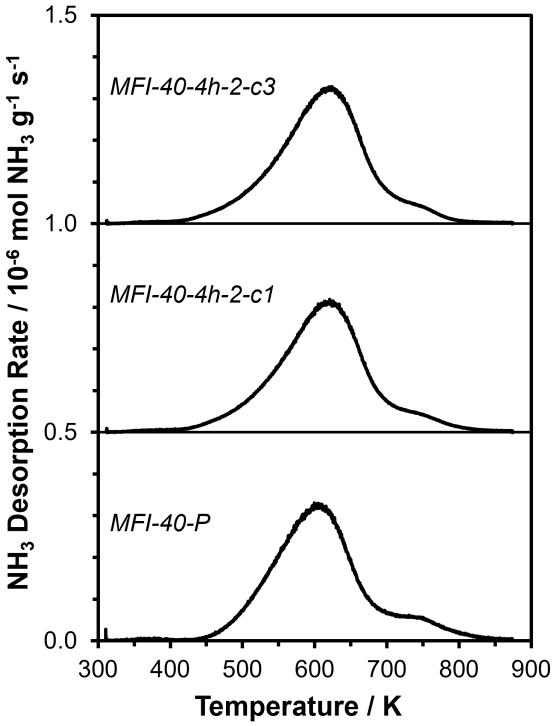

Figure S7. NH_3 TPD profiles on NH_4-form MFI-40-P, MFI-40-4h-2-c1 and MFI-40-4h-2-c3 samples. TPD profiles are vertically offset for clarity.

Section S6. 2,6-Di-*tert*-butylpyririne (DTBP) TPD Profiles of NH_4-form MFI Samples

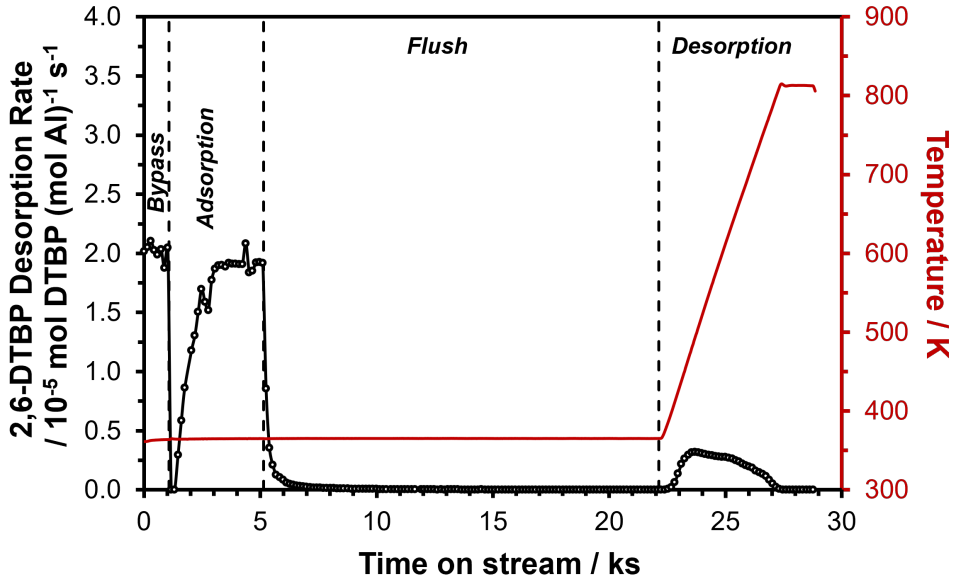

Figure S8. DTBP adsorption and desorption profile on MFI-13-P.

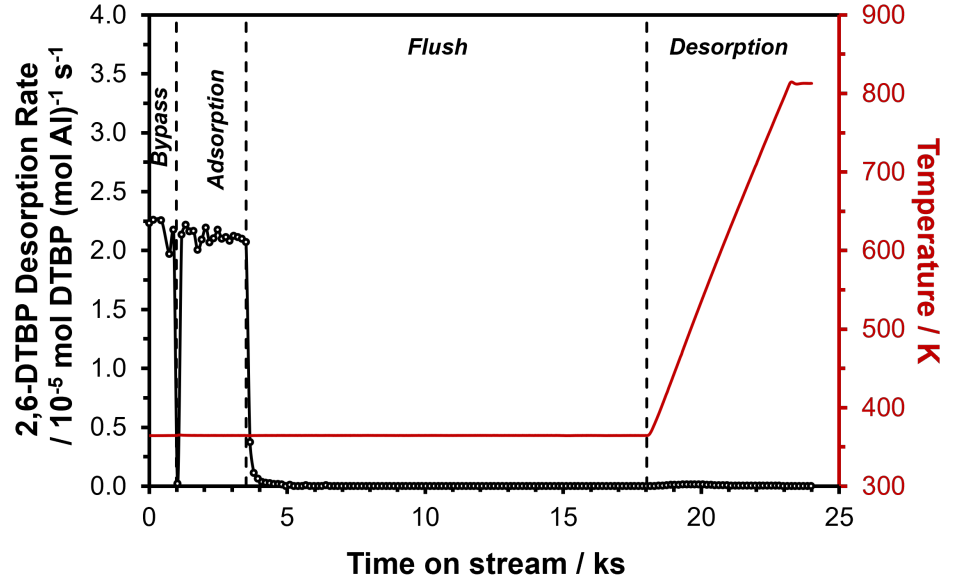

Figure S9. DTBP adsorption and desorption profile on MFI-13-4h-2-c3. Desorbed DTBP was below detection limits of the technique.

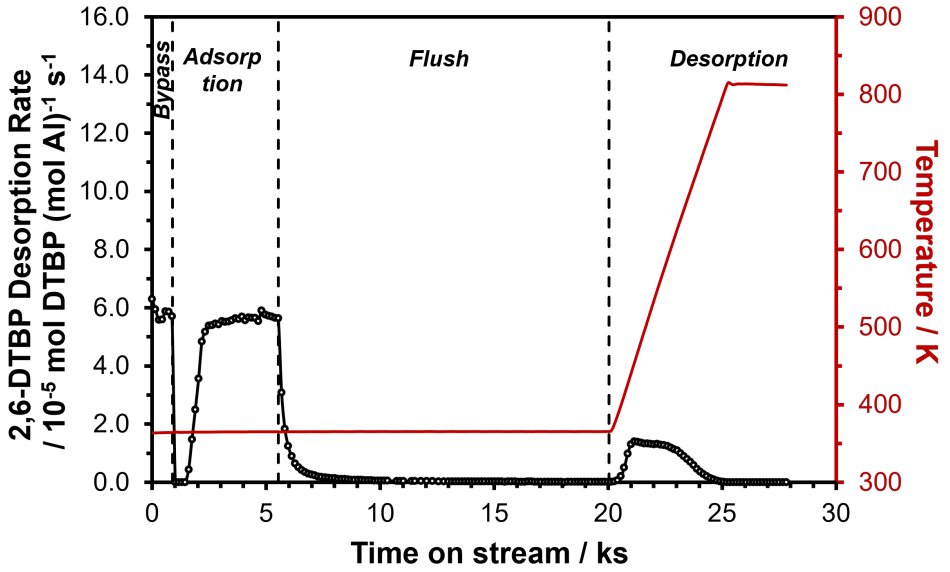

Figure S10. DTBP adsorption and desorption profile on MFI-40-P.

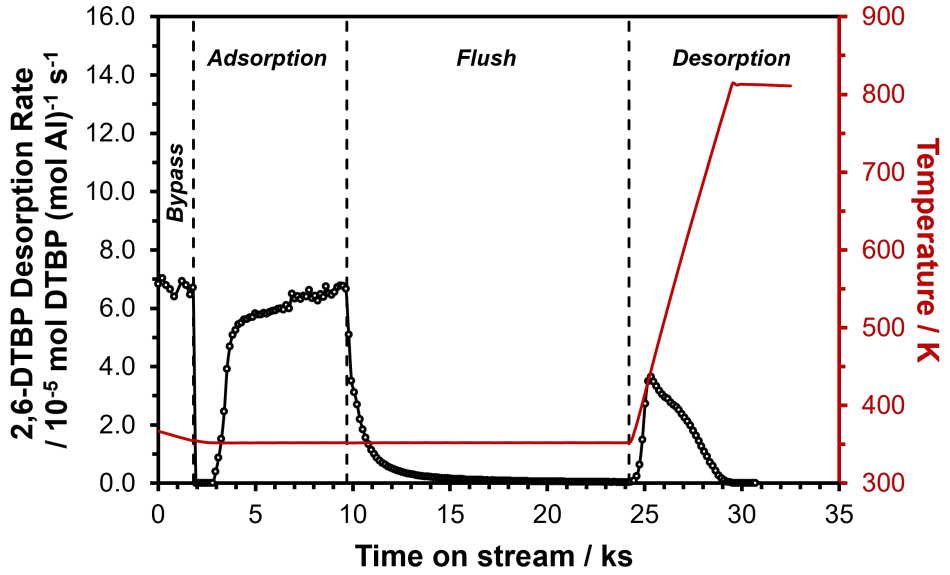

Figure S11. DTBP adsorption and desorption profile on MFI-C666.

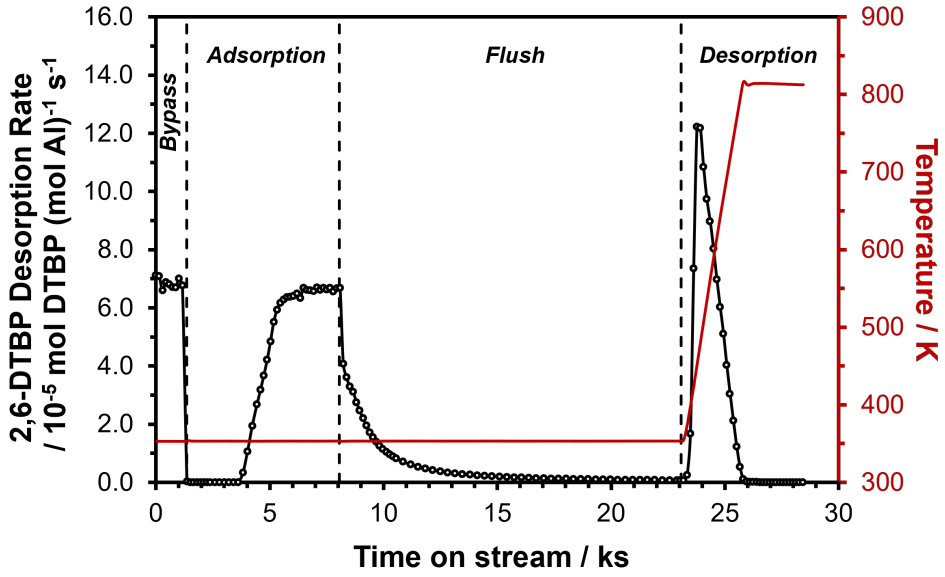

Figure S12. DTBP adsorption and desorption profile on MFI-C868.

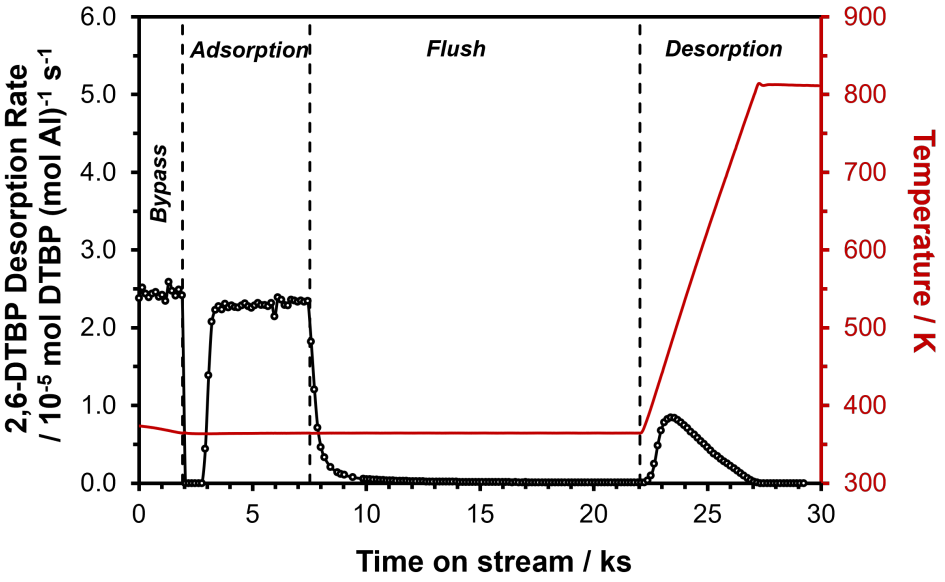

Figure S13 DTBP adsorption and desorption profile on MFI-16-P.

Section S7. XPS Analysis of MFI Samples

X-ray photoelectron spectroscopy (XPS) was performed at the Surface Analysis Facility of the Birck Nanotechnology Center (Purdue University) using a Kratos AXIS Ultra DLD Imaging spectrometer equipped with an Al Kα X-ray radiation source (1483.6 eV) operating at 75 W and 12 mins of acquisition time. The data were acquired while the sample was under high vacuum (P ~ 10^{-9} Torr) analyzed with CasaXPS software (version 2.3.25PR1.0)[14] and the binding energies on each sample were corrected for surface charging effects by setting the C 1s peak of the adventitious carbon to a binding energy of 284.8 eV. Surface elemental composition (Si/Al) was quantified using the integrated areas of the Si 2p and Al 2p peaks and the Scofield photoionization cross sections.[15,16]

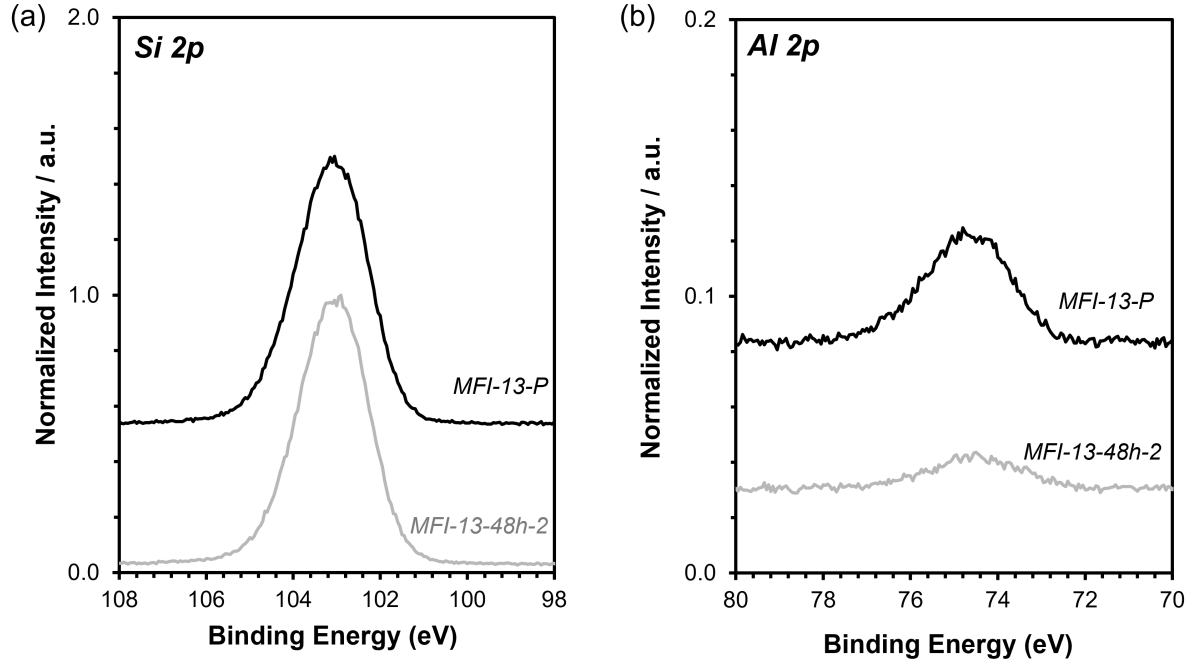

Figure S14. Peak intensities of the (a) Si 2p and (b) Al 2p binding energy regions in XPS spectra of MFI-13-P (black line) and MFI-13-48h-2 (gray line). Spectra were normalized to maximum Si 2p intensity for each sample. Spectra were vertically offset for clarity.

Table S3. Elemental composition of bulk and surface of MFI (up to 10 nm depth)

Sample	Bulk Si/Al[a] (ICP)	Surface Si/Al[b] (XPS)
MFI-13-P	12.5 ± 0.5	13 ± 2
MFI-13-48h-2	13.4 ± 1.3	39 ± 8

[a]Uncertainties in ICP quantification are ±10% (unless otherwise noted)
[b]Uncertainties in XPS quantification[17] are ±20%.

Section S8. Mechanisms for Mesitylene Benzylation Catalysis on Brønsted acid sites

Mesitylene benzylation can proceed via concerted (also known as direct or associative) or sequential (also known as indirect or dissociative or consecutive) mechanisms. The concerted mechanism (Equation S1 and S2) involves the direct reaction of co-adsorbed mesitylene (C_9H_{12}) with an undissociated benzylating agent ($ROCH_2C_6H_5$), either dibenzyl ether (DBE; R = $CH_2C_6H_5$) or benzyl alcohol (BA; R = H) at a zeolitic acid site (H^+Z^-):

$$ROCH_2C_6H_5 + H^+Z^- \rightarrow \left[ROH \cdots C_6H_5CH_2^{\delta+} \cdots Z^{\delta-}\right]^{\ddagger} \rightarrow ROH + C_6H_5CH_2^{\delta+}-Z^{\delta-} \quad \text{(S1)}$$

$$C_9H_{12} + C_6H_5CH_2^{\delta+}-Z^{\delta-} \rightarrow \left[C_9H_{12} \cdots C_6H_5CH_2^{\delta+} \cdots Z^{\delta-}\right]^{\ddagger} \rightarrow C_{16}H_{18} + H^+Z^- \quad \text{(S2)}$$

In contrast, the sequential mechanism (Equation S3) involves the initial benzylation of the H^+ site by DBE (or BA) to form a surface benzyl species while liberating BA (or H_2O in the case of BA) and the subsequent reaction of the surface benzyl group with a physisorbed mesitylene:

$$\begin{aligned} ROCH_2C_6H_5 + C_9H_{12} + H^+Z^- &\rightarrow \left[ROH \cdots C_6H_5CH_2^{\delta+} \cdots C_9H_{12} \cdots Z^{\delta-}\right]^{\ddagger} \\ &\rightarrow ROH + C_{16}H_{18} + H^+Z^- \end{aligned} \quad \text{(S3)}$$

The two mechanisms differ because surface benzyl species are reactive intermediates in the sequential pathway, but not in the concerted pathway. However, *in situ* spectroscopic experiments are often unable to distinguish between both mechanisms during aromatic alkylation because the presence, absence, or abundance of surface alkoxy species (e.g., $C_6H_5CH_2$–Z) does not preclude either mechanism, since such species may be highly reactive and consumed too rapidly to be observed or be essentially unreactive (relative to $ROCH_2C_6H_5$) and present as spectators. Moreover, kinetic experiments are often unable to identify the prevailing mechanisms because rate expressions derived from either mechanism can have similar dependences on concentrations of aromatic and alkylating reactants. Theoretical studies have noted that both aromatic alkylation mechanisms can occur but that the dominant mechanism depends on the reaction temperatures, reactant concentrations, conversion and zeolite topology.[18–23]

S8.1. *Derivation of the concerted mesitylene benzylation rate expression*

We propose a sequence of elementary steps (Scheme S2) for mesitylene benzylation on external H^+ sites via the concerted mechanism. The abridged derivation is presented in the main text (Section 3.2.2) while the full derivation is presented here. The choice of the concerted mechanism in the main text was predicated on the high mesitylene to benzylating agent molar

ratios (>20:1), the high concentrations of mesitylene relative to total Al in the zeolite catalyst (TMB/Al_{total} molar ratio > 1000), and the relatively low reaction temperatures (363 K).

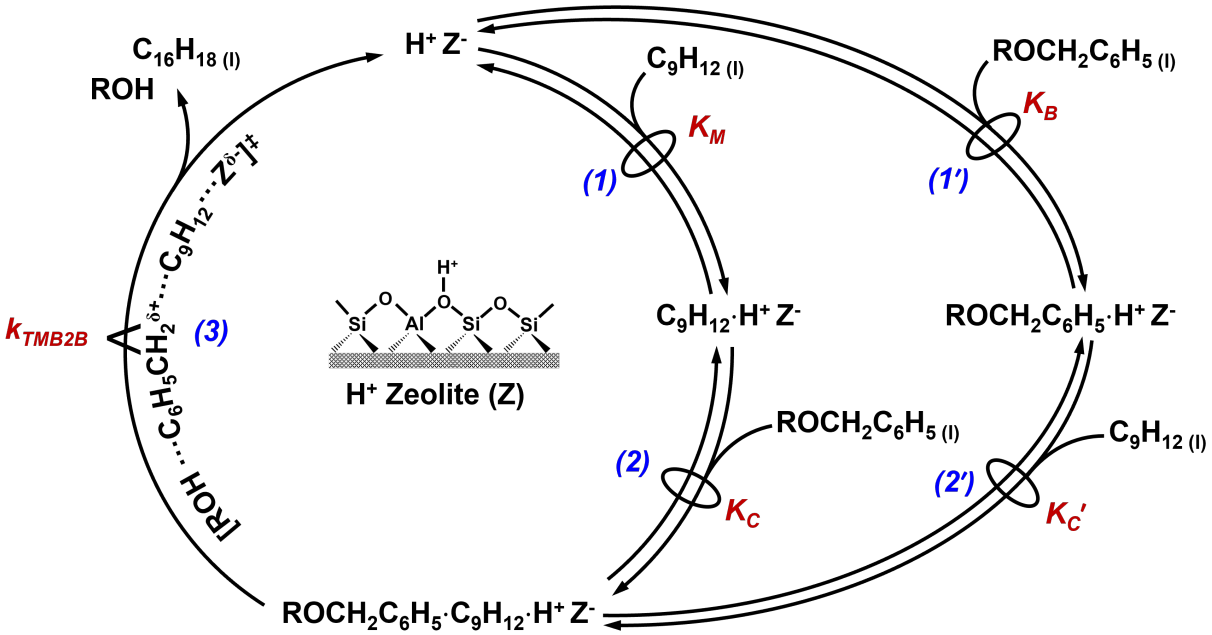

Scheme S2. Proposed full reaction mechanism (via concerted pathway) for benzylation of mesitylene (C_9H_{12}) with a benzylating agent ($ROCH_2C_6H_5$) on a Brønsted acid site (H^+Z^-) to form 1,3,5 trimethyl-2-benzylbenzene ($C_{16}H_{18}$) and a leaving group (ROH). Steps (1′) and (2′) are added to steps 1–3 in Scheme 2 (main text) to account for adsorption of benzylating species on H^+Z^-.

The reaction sequence begins with the quasi-equilibrated adsorption of mesitylene from the bulk extracrystalline solvent phase ($C_9H_{12(l)}$) to the active site (H^+Z^-) (Step 1). This is followed by the quasi-equilibrated adsorption of benzylating species from the extracrystalline solvent phase ($ROCH_2C_6H_{5(l)}$ or $BzOR_{(l)}$) onto the adsorbed mesitylene ($C_9H_{12}{\cdot}H^+Z^-$) to form a co-adsorbed complex ($C_9H_{12}{\cdot}ROCH_2C_6H_5{\cdot}H^+Z^-$) (Step 2). Alternatively, the quasi-equilibrated adsorption of the benzylating species ($ROCH_2C_6H_5{\cdot}H^+Z^-$) can occur (Step 1′) followed by the quasi-equilibrated adsorption of mesitylene to form the co-adsorbed complex (Step 2′). Following the formation of the co-adsorbed complex, the irreversible and kinetically relevant C–C bond formation (Step 3) between a 2-carbon of mesitylene and the benzylic carbon of DBE (or BA) forms 1,3,5 trimethyl-2-benzylbenzene ($C_{16}H_{18}{\cdot}H^+Z^-$) and the associated leaving group of the benzylating agent (ROH); both species desorb from the active site and into the bulk extracrystalline solvent phase ($C_{16}H_{18(l)}$, $ROH_{(l)}$) thereby closing the catalytic cycle. Steps involving the deprotonation of 1,3,5 trimethyl-2-benzylbenzenium ($C_{16}H_{19}{}^+Z^-$) and proton transfer back to the zeolite are omitted due to the

known kinetic irrelevance of the deprotonation step during aromatic alkylations.[20,24] In Scheme S2, K_M is the equilibrium constant for adsorption of mesitylene from the solution phase to the active site, K_C is the equilibrium constant for forming the co-adsorbed mesitylene–DBE (or mesitylene–BA) complex from a DBE (or BA) molecule in the solvent phase and an adsorbed mesitylene, K_B is the equilibrium constant for adsorption of benzylating species from the bulk solution phase to the active site, K_C' is the equilibrium constant for forming the co-adsorbed mesitylene–DBE (or BA) complex from a mesitylene molecule in the solvent phase and an adsorbed DBE (or BA), and k_{TMB2B} is the rate constant for the kinetically relevant step that forms the C–C bond formation transition state from the relevant precursor state.

The mesitylene benzylation rate (r_{TMB2B}) can be written as the net rate of a non-equilibrated step (Step 3), which was taken here as the irreversible and kinetically relevant C–C bond formation within the co-adsorbed surface intermediate:

$$r_{TMB2B} = k_{TMB2B}\,[\mathrm{ROCH_2C_6H_5 \cdot C_9H_{12} \cdot H^+Z^-}] \tag{S4}$$

The concentrations of the surface species can be expressed in terms of the concentrations of unoccupied acid sites ($[H-Z]$) and the thermodynamic activities of reactants species in the bulk extracrystalline liquid phase (a_{BzOR} and a_{TMB}), because reactant adsorption-desorption steps are assumed to be quasi-equilibrated.

$$[\mathrm{C_9H_{12} \cdot H^+Z^-}] = K_M a_{TMB}[\mathrm{H^+Z^-}] \tag{S5}$$

$$[\mathrm{ROCH_2C_6H_5 \cdot H^+Z^-}] = K_B a_{BzOR}[\mathrm{H^+Z^-}] \tag{S6}$$

$$[\mathrm{ROCH_2C_6H_5 \cdot C_9H_{12} \cdot H^+Z^-}] = K_C K_M a_{TMB} a_{BzOR}[\mathrm{H^+Z^-}] \tag{S7}$$

$$[\mathrm{ROCH_2C_6H_5 \cdot C_9H_{12} \cdot H^+Z^-}] = K_C{}' K_B a_{TMB} a_{BzOR}[\mathrm{H^+Z^-}] \tag{S8}$$

However, only three steps out of 1, 1′, 2 and 2′ (Scheme S2) are linearly independent and needed for the rate derivation; for example, K_C' can be expressed in terms of the other adsorption constants:

$$K_C' = \frac{K_C K_M}{K_B} \tag{S9}$$

Thus, Equation S4 can be re-written in terms of concentrations of unoccupied sites on the catalyst and thermodynamic activities of reactants in the bulk extracrystalline liquid phase:

$$r_{TMB2B} = k_{TMB2B}\, K_C K_M a_{TMB} a_{BzOR} [\mathrm{H^+Z^-}] \quad \text{(S10)}$$

At the low concentrations of benzylating species in TMB (~1–8 vol %;), the solution-phase activity coefficients are expected to approach unity (i.e., $\gamma_i \rightarrow 1$) and ideal solution behavior was assumed. Thus, thermodynamic activities (a_i) can be replaced with concentrations (C_i) referenced to the standard concentration (C^0 = 1 mol m^{-3}) :

$$a_i = \gamma_i \frac{C_i}{C^0} \quad \text{(S11)}$$

A site balance is used to determine the concentration of unoccupied active sites in terms of the concentration of active sites ($[L]$) available for mesitylene benzylation regardless of their state (unoccupied or occupied by guest species).

$$[L] = [H-Z] + [\mathrm{C_9H_{12}} \cdot \mathrm{H^+Z^-}] + [\mathrm{ROCH_2C_6H_5} \cdot \mathrm{H^+Z^-}] + [\mathrm{ROCH_2C_6H_5} \cdot \mathrm{C_9H_{12}} \cdot \mathrm{H^+Z^-}] \quad \text{(S12)}$$

The concentrations of surface species (Equations S5–S7) can be substituted into Equation S11, which upon rearranging, yields:

$$[H-Z] = \frac{1}{1 + K_M C_{TMB} + K_B C_{BzOR} + K_C K_M C_{TMB} C_{BzOR}} [L] \quad \text{(S13)}$$

The rate expression (Equation S10) can thus be re-written in terms of the concentrations of reactants and total concentration of active sites available for mesitylene benzylation:

$$r_{TMB2B} = \frac{k_{TMB2B} K_C K_M C_{TMB} C_{BzOR}}{1 + K_M C_{TMB} + K_B C_{BzOR} + K_C K_M C_{TMB} C_{BzOR}} [L] \quad \text{(S14)}$$

The denominator terms in Equation S14 respectively represent ratios (relative to [H^+Z^-]) of concentrations of unoccupied Brønsted acid sites ([H–Z]), adsorbed mesitylene ([C_9H_{12}·H^+Z^-], adsorbed benzylating species ([$ROCH_2C_6H_5$·H^+Z^-]) and co-adsorbed mesitylene–benzylating agent ([C_9H_{12}·$ROCH_2C_6H_5$·H^+Z^-]). At the high molar ratios of mesitylene relative to benzylating agent (>20:1) or total Al sites (>1000), the mesitylene-derived species (adsorbed mesitylene and co-adsorbed mesitylene–DBE (or mesitylene–BA)) are assumed to be the two most abundant reactive intermediates (MARIs) and mesitylene benzylation rates have a zero-order dependence on mesitylene concentrations (~7000 mol m^{-3}). Furthermore, the concentrations of TMB2B and

leaving group of the benzylating species (ROH) are assumed to be negligible at low reactant conversions (X_{TMB} < 0.1%, X_{BzOR} < 10%). Thus, Equation S14 can be simplified:

$$r_{TMB2B} = \frac{k_{TMB2B} K_C K_M C_{TMB} C_{BzOR}}{K_M C_{TMB} + K_C K_M C_{TMB} C_{BzOR}} [L] \quad \text{(S15)}$$

Equation S15 can be recast to the following form:

$$r_{TMB2B} = \frac{k_{TMB2B} K_C C_{BzOR}}{1 + K_C C_{BzOR}} [L] \quad \text{(S16)}$$

As the concentrations of benzylating agent in the bulk TMB solution phase decreases towards infinite dilution, mesitylene benzylation rates are expected to approach a first-order dependence in the concentration of benzylating agent:

$$r_{TMB2B} = k_{TMB2B} K_C C_{BzOR} [L] \quad \text{(S17)}$$

while at sufficiently high concentrations of benzylating agent, measured rates become independent of the concentration of benzylating agent and reflect the zero-order rate constant (k_{TMB2B}):

$$r_{TMB2B} = k_{TMB2B} [L] \quad \text{(S18)}$$

Furthermore, in the zero-order kinetic regime (with respect to both the benzylating species and mesitylene), all accessible active sites (i.e., L) are saturated with the co-adsorbed intermediate as the sole MARI:

$$[L] \approx [\mathrm{ROCH_2C_6H_5 \cdot C_9H_{12} \cdot H^+Z^-}] \quad \text{(S19)}$$

The total number of active sites ($[L]$) that stabilize mesitylene benzylation transition states is strictly proportional to the concentrations of external acid sites ($[H^+_{ext}]$). Thus, measured reaction rates (mol TMB2B formed per unit time per mol Al_{total}) in the zero-order kinetic regime reflect the product of the intrinsic rate constant for benzylation at external H^+ sites (mol TMB2B formed per unit time per mol H^+_{ext}) and the fraction of external acid sites (mol H^+_{ext} per mol Al_{total}).

$$r_{TMB2B} = k_{TMB2B} [H^+_{ext}] \quad \text{(S20)}$$

Furthermore, using transition state theory[25,26], the zero-order mesitylene benzylation rate constant can be expressed in terms of the Gibbs free energy difference between the kinetically relevant transition states and the precursor state:

$$k_{TMB2B} = \frac{k_B T}{h} e^{\frac{-(\Delta G_{\ddagger}^{o} - \Delta G^{o}_{\mathrm{ROCH_2C_6H_5 \cdot C_9H_{12} \cdot H^+Z^-}})}{RT}} = \frac{k_B T}{h} e^{\frac{-\Delta G_{act}}{RT}} \quad \text{(S21)}$$

In contrast to micropores of molecular dimensions (< ~2 nm diameter) that can confine active sites, intermediates and transition states within them,[27] the external surfaces or mesoporous regions of zeolite crystallites (>~2 nm diameter) are too large to effectively confine and influence the free energies of the kinetically relevant transition states and intermediates involved in mesitylene benzylation (minimum diameter ~ 0.7 nm, maximum length ~ 1.2 nm)[28,29]. Furthermore, theoretical studies have shown that the acid strength of external Brønsted acid sites, as defined by their deprotonation energies (i.e., energy required to remove a proton to non-interacting distances), is similar to that of internal Brønsted acid sites.[30,31] Prior experimental studies[32–34] have also suggested that external H^+ sites are similarly reactive (within 3×) for mesitylene benzylation on various MFI samples possessing conventional, nanosheet or hierarchical structures. Minor variations in rate constants among MFI samples have been attributed to differences in morphologies, surface roughness, surface silanol defects and Al distribution, as well as effects of partial confinement on surface pockets formed by the termination of micropores.[31,34] Thus, under zero-order kinetic regimes, kinetically-controlled rates of mesitylene benzylation at a given temperature should only depend, to a first approximation, on the concentration of external acid sites in MFI:

$$r_{TMB2B} \cong \frac{k_B T}{h} e^{\frac{-(\Delta G_{\ddagger}^{o} - \Delta G^{o}_{\mathrm{ROCH_2C_6H_5 \cdot C_9H_{12} \cdot H^+Z^-}})}{RT}} [H^+_{ext}] \quad \text{(S22)}$$

Next, we derive the sequential mesitylene benzylation rate expression to show that a zero-order rate constant can also be recovered and that the observed dependence of k_{TMB2B} (per total Al) on $[H^+_{ext}]$ (per total Al) does not depend on the choice of the prevalent mechanism

S8.2. *Derivation of the sequential mesitylene benzylation rate expression*

We propose a sequence of elementary steps (Scheme S3) for mesitylene benzylation on external H^+ sites via the sequential mechanism. The derivation follows an approach similar to that of the concerted mechanism (Section S8.1). The sequential mechanism begins with the quasi-equilibrated adsorption of the benzylating species from the bulk liquid-phase to the H^+ site (Step I) and subsequent benzylation of the H^+ site to form a surface benzyl species while liberating the associated ROH leaving group (Step II). The reaction further proceeds with quasi-equilibrated co-

adsorption of a mesitylene from the bulk liquid phase onto the surface benzyl group (Step III) and the subsequent kinetically relevant C–C bond formation to produce TMB2B and close the catalytic cycle (Step IV). The quasi-equilibrated adsorption of mesitylene from the bulk liquid-phase to the active site (Step 1′) is included as an off-cycle step to account for the possible occupancy of active sites by adsorbed mesitylene.

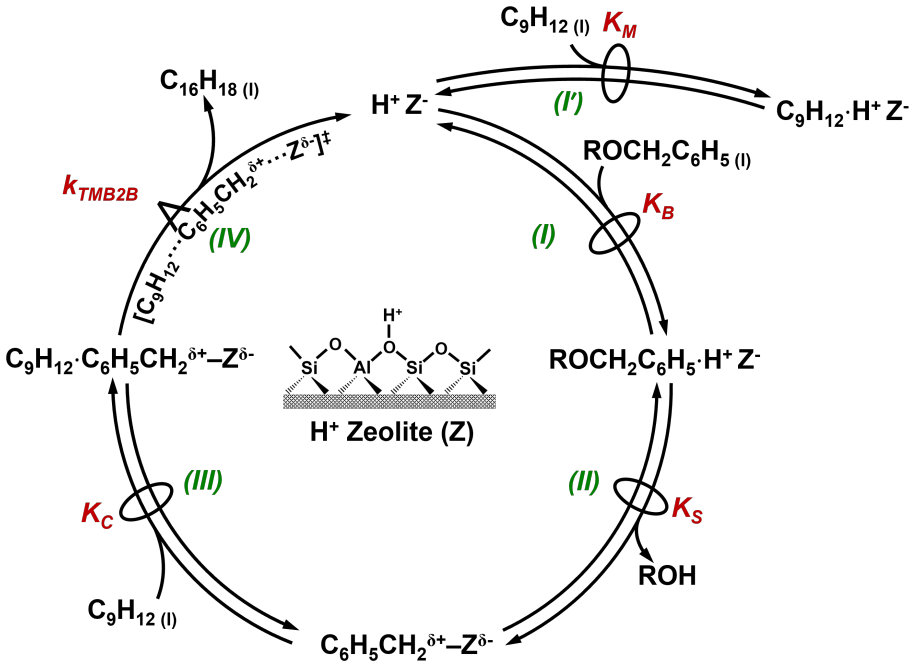

Scheme S3. Proposed full reaction mechanism (via sequential pathway) for benzylation of mesitylene (C_9H_{12}) with a benzylating agent ($ROCH_2C_6H_5$) on a Brønsted acid site (H^+Z^-) to form 1,3,5 trimethyl-2-benzylbenzene ($C_{16}H_{18}$) and a leaving group (ROH).

In Scheme S3, K_B is the equilibrium constant for adsorption of benzylating species from the bulk solution phase to the active site, K_S is the equilibrium constant for benzylation of the active site, K_C is the equilibrium constant for forming the co-adsorbed mesitylene–surface benzyl species from a DBE (or BA) molecule in the solvent phase and an adsorbed mesitylene, K_M is the equilibrium constant for adsorption of mesitylene from the bulk solution phase to the active site and k_{TMB2B} is the rate constant for the kinetically relevant step that forms the C–C bond formation transition state from the relevant precursor state. The mesitylene benzylation rate (r_{TMB2B}) can be written as the irreversible and kinetically relevant C–C bond formation (Step IV):

$$r_{TMB2B} = k_{TMB2B}\left[\mathrm{C_9H_{12}} \cdot \mathrm{C_6H_5CH_2^{\delta+}} - \mathrm{Z^{\delta-}}\right] \quad \text{(S23)}$$

The concentrations of the surface species can be expressed in terms of the concentrations of unoccupied acid sites ($[H-Z]$) and the bulk liquid-phase concentrations of reactants (c_{BzOR}, C_{TMB}) and product (C_{BzOR}):

$$[\mathrm{ROCH_2C_6H_5} \cdot \mathrm{H^+Z^-}] = K_B C_{BzOR}[\mathrm{H^+Z^-}] \quad \text{(S24)}$$

$$\left[\mathrm{C_6H_5CH_2^{\delta+}}{-}\mathrm{Z^{\delta-}}\right] = K_B K_S \frac{C_{BzOR}}{C_{ROH}}\ [\mathrm{H^+Z^-}] \quad \text{(S25)}$$

$$\left[\mathrm{C_9H_{12}} \cdot \mathrm{C_6H_5CH_2^{\delta+}} - \mathrm{Z^{\delta-}}\right] = K_C K_B K_S \frac{C_{BzOR}}{C_{ROH}} C_{TMB}\ [\mathrm{H^+Z^-}] \quad \text{(S26)}$$

$$[\mathrm{C_9H_{12}} \cdot \mathrm{H^+Z^-}] = K_M C_{TMB}[\mathrm{H^+Z^-}] \quad \text{(S27)}$$

Using Equations S24–S27, Equation S23 can be re-written in terms of concentrations of unoccupied sites, reactants and ROH leaving group:

$$r_{TMB2B} = k_{TMB2B}\, K_C K_B K_S \frac{C_{BzOR}}{C_{ROH}} C_{TMB}\ [\mathrm{H^+Z^-}] \quad \text{(S28)}$$

A site balance is on all active sites yields:

$$[L] = [H-Z] + [\mathrm{C_9H_{12}} \cdot \mathrm{H^+Z^-}] + [\mathrm{ROCH_2C_6H_5} \cdot \mathrm{H^+Z^-}] + \left[\mathrm{C_6H_5CH_2^{\delta+}}{-}\mathrm{Z^{\delta-}}\right] + \left[\mathrm{C_9H_{12}} \cdot \mathrm{C_6H_5CH_2^{\delta+}} - \mathrm{Z^{\delta-}}\right] \quad \text{(S29)}$$

Upon substitution of Equations S24–S27 into Equation S29 and subsequent rearrangement, the concentration of unoccupied sites can be expressed in terms of equilibrium constants and concentrations of reactants and ROH leaving group:

$$[H-Z] = \frac{1}{1 + K_M C_{TMB} + K_B C_{BzOR} + K_B K_S \frac{C_{BzOR}}{C_{ROH}} + K_C K_B K_S \frac{C_{BzOR}}{C_{ROH}} C_{TMB}}[L] \quad \text{(S30)}$$

Equation S28 can be re-written to obtain the full rate expression in terms of rate constants, equilibrium constants and measurable reactant concentrations and ROH product concentrations:

$$r_{TMB2B} = \frac{k_{TMB2B}\, K_C K_B K_S \frac{C_{BzOR}}{C_{ROH}} C_{TMB}}{1 + K_M C_{TMB} + K_B C_{BzOR} + K_B K_S \frac{C_{BzOR}}{C_{ROH}} + K_C K_B K_S \frac{C_{BzOR}}{C_{ROH}} C_{TMB}}\ [L] \quad \text{(S31)}$$

The denominator terms in Equation S31 respectively represent ratios (relative to $[H^+Z^-]$) of concentrations of unoccupied Brønsted acid sites, adsorbed mesitylene, adsorbed benzylating species, surface benzyl species, and co-adsorbed mesitylene–surface benzyl species. The full rate expression for mesitylene benzylation via the sequential route can be further simplified by considering the operating reaction conditions. At high molar ratios of mesitylene relative to benzylating agent (>20:1) or total Al sites (>1000), the concentrations of adsorbed (and undissociated) benzylating species and unoccupied H^+ sites are negligible. The rate expression can be simplified to:

$$r_{TMB2B} = \frac{k_{TMB2B}\, K_C K_B K_S \frac{C_{BzOR}}{C_{ROH}} C_{TMB}}{K_M C_{TMB} + K_B K_S \frac{C_{BzOR}}{C_{ROH}} + K_C K_B K_S \frac{C_{BzOR}}{C_{ROH}} C_{TMB}} [L] \quad \text{(S32)}$$

However, as shown in Equation S32, the concentration of surface benzyl species (second denominator term; relative to $[H^+Z^-]$) depends not only on the relative concentrations of benzylating species in the bulk liquid phase, but also depends on the concentration of the ROH leaving group and hence the conversion of benzylating species (X_{BzOR}). At low bulk concentrations of benzylating species, rates predicted by the sequential mechanism approach a first-order dependence in concentration of benzylating species but have a negative first-order dependence on the concentration of the ROH leaving group, consistent with insights from a previous study[20]:

$$r_{TMB2B} = \frac{k_{TMB2B}\, K_C K_B K_S \frac{C_{BzOR}}{C_{ROH}} C_{TMB}}{K_M C_{TMB}} [L] = k_{TMB2B} \frac{K_C K_B K_S}{K_M} \frac{C_{BzOR}}{C_{ROH}} [L] \quad \text{(S33)}$$

In contrast, at sufficiently high bulk concentrations of benzylating species (in excess mesitylene), mesitylene benzylation rates via a sequential mechanism will approach a zero-order dependence in benzylating species because the surface is covered with co-adsorbed mesitylene and surface benzyl species:

$$r_{TMB2B} = \frac{k_{TMB2B}\, K_C K_B K_S \frac{C_{BzOR}}{C_{ROH}} C_{TMB}}{K_C K_B K_S \frac{C_{BzOR}}{C_{ROH}} C_{TMB}} [L] = k_{TMB2B}[L] \quad \text{(S34)}$$

Thus, in the zero-order kinetic regime (with respect to benzylating species and mesitylene), the mesitylene benzylation rate expressions via sequential mechanism (Equation S34) are the same

functional form as that via the concerted mechanism (Equation S18), with the exception that all accessible active sites in the concerted mechanism are covered by a co-adsorbed mesitylene–DBE (or mesitylene–BA) as the MARI (Equation S19), whereas all accessible sites in the sequential mechanism are covered by co-adsorbed mesitylene–surface benzyl species as the MARI:

$$[L] \approx \left[C_9H_{12} \cdot C_6H_5CH_2^{\delta+} - Z^{\delta-}\right] \tag{S35}$$

Therefore, irrespective of the choice of prevalent reaction mechanism, measured rates reflect the product of the intrinsic rate constant and concentrations of external acid sites (Equation S20).

Section S9. Mesitylene Benzylation Kinetic Measurements

S9.1. *Measurement of mesitylene benzylation rates from TMB2B concentration profiles*

The liquid-phase concentration of TMB2B and the mesitylene conversion is shown as a function of batch reaction time during mesitylene benzylation (363 K) with DBE on MFI-40-P (Figure S15a). The molar ratios of BA to TMB2B and to DBE are shown in Figure S15b. Equimolar BA and TMB2B concentrations are expected for DBE reactions with mesitylene; however, BA/TMB2B molar ratios greater than unity are proposed to result from background DBE hydrolysis by trace amounts of adventitious H_2O at internal H^+ sites. Nevertheless, contributions of BA to mesitylene benzylation are expected to be negligible because of the low BA/DBE ratios throughout the reaction time course.

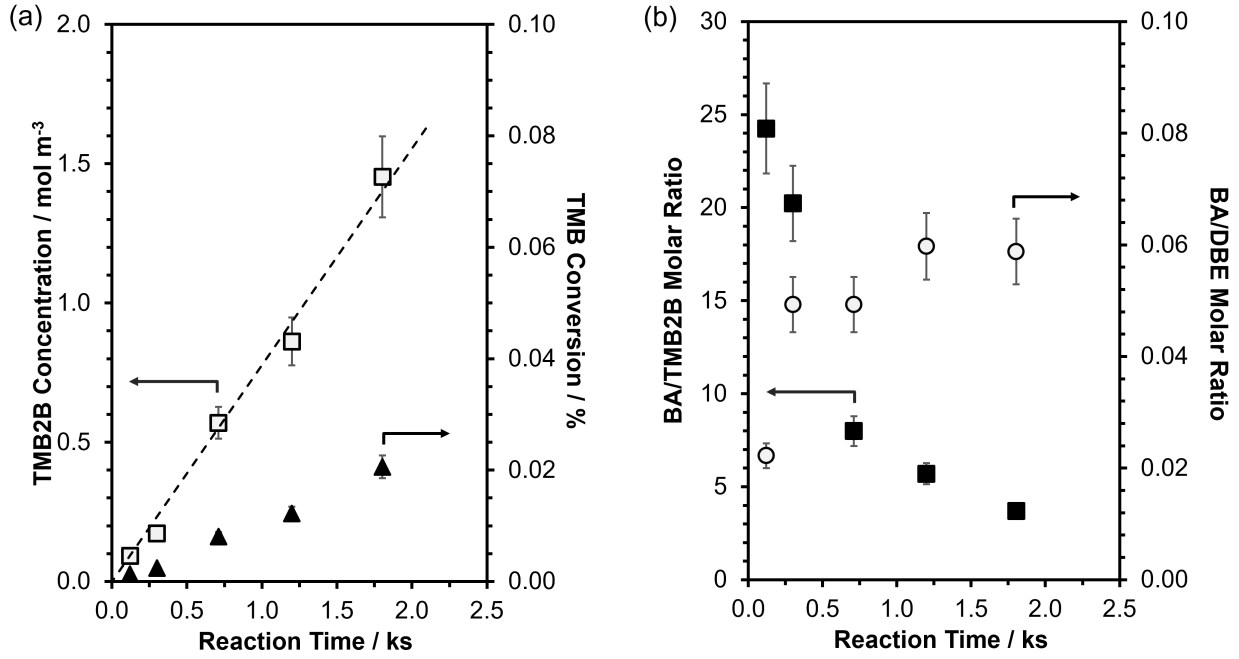

Figure S15. (a) Concentrations of TMB2B (□) and percent TMB conversion to TMB2B (▲) as a function of batch reaction time during mesitylene benzylation (363 K) with DBE (b) Molar ratios of BA to TMB2B (■) and BA to DBE (○) as a function of batch reaction time during mesitylene benzylation (363 K) with DBE on MFI-40-P (TMB:DBE molar ratio = 75:1; DBE/Al molar ratio = 25).

Initial rates of mesitylene benzylation by DBE (r_{TMB2B}; per total Al) were estimated by fitting temporal TMB2B concentration (C_{TMB2B}) profiles during mesitylene benzylation with DBE or BA at low reactant conversions ($X_{TMB} < 0.1\%$, and X_{DBE} or $X_{BA} < 10\%$) to a differential (well-mixed) batch reactor model. Differential rate measurements are typically preferred when the rate expressions (i.e., dependence of rates on reactant and product concentrations) are to be determined.

The balance on the number of moles of TMB2B product (N_{TMB2B}) in a well-mixed batch reactor at constant volume of reactant solution ($V_{solution}$) containing a given number of Al sites (N_{Al}) can be expressed as:

$$\frac{1}{V_{solution}}\frac{dN_{TMB2B}}{dt} = \frac{dC_{TMB2B}}{dt} = r_{TMB2B}\frac{N_{Al}}{V_{solution}} \tag{S36}$$

Rearrangement and separation of variables yields:

$$dC_{TMB2B} = r_{TMB2B}\frac{N_{Al}}{V_{solution}}dt \tag{S37}$$

Further integrating the left side from C_{TMB2B} = 0 to C_{TMB2B} and the right side from t = 0 to t, and assuming that the reaction rates change negligibly with time (i.e., under differential conditions), the concentration of TMB2B product can be expressed as a function of batch reaction time:

$$C_{TMB2B}(t) = r_{TMB2B}\left(\frac{N_{Al}}{V_{solution}}\right)t \tag{S38}$$

Thus, the mesitylene benzylation rates (r_{TMB2B}) can be estimated by dividing the slope from the linear regression (with zero intercept) of measured TMB2B concentration ($C_{TMB2B}(t)$) as a function of batch reaction time (t) by the number of moles of Al per volume of solution $\left(\frac{N_{Al}}{V_{solution}}\right)$.

Differential measurements can also be confirmed by varying the catalyst-to-solution ratio and showing that the mesitylene benzylation rates are similar within the experimental uncertainty (±20%). This can be shown by plotting the TMB2B concentration against contact time (defined as $\left(\frac{N_{Al}}{V_{solution}}t\right)$) during mesitylene benzylation by BA (363 K) on MFI-40-P (Figure S16), which gives slopes that are equal to the mesitylene benzylation rates.

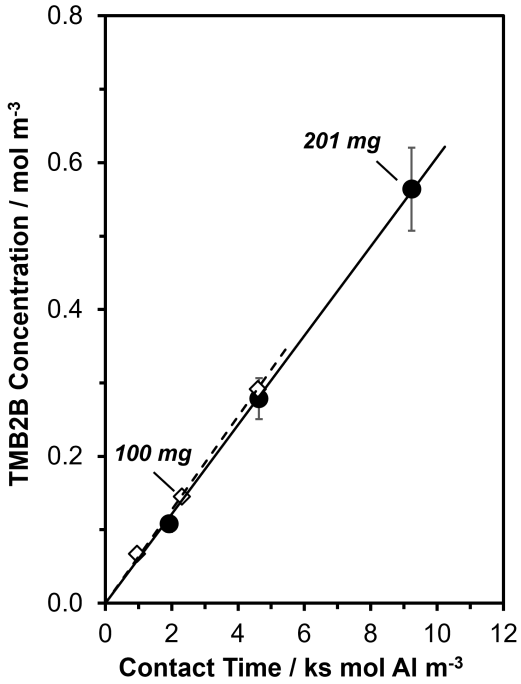

Figure S16. Dependence of liquid-phase concentrations of TMB2B on contact time during mesitylene benzylation (363 K) with BA on MFI-40-P (Initial BA concentration ≈ 200 mol m^{-3}; TMB:BA molar ratio 40:1) at varying ratios of catalyst mass to volume of solution (100 (◇) or 201 (●) mg per 5.1 cm^3). TMB2B were sampled at batch reaction times ranging between 0.13–0.60 ks.

S9.2. *Assessment of extracrystalline transport limitations on measured mesitylene benzylation rates*

For mesitylene benzylation to occur at acid sites at extracrystalline surfaces, mesitylene and DBE (or BA) reactants must diffuse from the bulk solution phase to the surface of the catalyst aggregates (interpellet) and then diffuse further to the external surface of the catalysts where the active sites are located (intrapellet). Rigorous rate comparisons among catalyst samples require that measured rates reflect the intrinsic kinetic behavior from surface reactions at acid sites at external crystallite surfaces, uncorrupted by extracrystalline transport phenomena. Interpellet concentration gradients can be minimized by stirring at a high enough speed to increase the external mass transfer coefficient of the reactants through the boundary layer surrounding catalyst aggregates.[35] We fulfilled this requirement by stirring our reaction mixture at higher rates (~900 rpm) than those (~500 rpm) in previous studies,[32–34,36] which reported that rates of mesitylene benzylation (with BA; per external H^+; 343 K) varied within a factor of 3× for various MFI samples

possessing conventional, nanosheet or hierarchical structures and possessing effective crystallite sizes spanning 3 orders of magnitude.

In addition, the Koros-Nowak test is a useful diagnostic criterion to evaluate potential influences of intrapellet transport limitations on measured rates.[37] If intrapellet diffusion constraints are significant, then measured rates (per total Al or per g catalyst) should decrease as the number of active sites per unit of pellet volume is increased. The strictly linear dependence of the zero-order mesitylene-benzylation rate constants (per total Al; 363 K) on the fraction of external H^+ sites (per total Al) provide further evidence that our reaction conditions and reactor hydrodynamics allow for the measurement of intrinsic rates. Furthermore, by showing that measured mesitylene benzylation rates (per total Al) are strongly a function of external H^+ (per total Al) at a temperature (363 K) different from that in previous studies (343 K), we also fulfilled the Madon-Boudart criterion[38] that further requires that exothermic reactions be evaluated at a different temperature to truly satisfy the Koros-Nowak criterion. Thus, we conclude that the rates (and rate constants) reported in this work reflect intrinsic kinetic behavior at external H^+ sites uncorrupted by interpellet or intrapellet transport artifacts.

Section S10. Summary of Measured Mesitylene Benzylation Rates and Estimated Concentrations of External Acid Sites

Table S4 Site characterization of MFI samples used in this study (normalized by sample mass)

Sample[a]	$k_{TMB2B,meas}$[a] (363 K) / 10^{-3} mol TMB2B (mol Al_{total})$^{-1}$ s^{-1}	H^+_{ext}[b] / 10^{-3} mol DTBP g^{-1}	H^+_{ext}[c] / 10^{-3} mol H^+_{ext} g^{-1}
MFI-13-P	0.0313	0.012	0.0086
MFI-13-4h-1	-	-	-
MFI-13-48h-1	-	-	-
MFI-13-4h-2	-	-	-
MFI-13-48h-2	-	-	-
MFI-13-4h-2-c1	0.0147	-	0.0038
MFI-13-4h-2-c2	0.0007	-	0.0002
MFI-13-4h-2-c3	0.0005	<0.001	0.0001
MFI-16-P	0.0070	0.021	0.0015
MFI-16-4h-2-c1	0.0033	-	0.0005
MFI-16-4h-2-c2	-	-	-
MFI-16-4h-2-c3	0.0016	-	0.0002
MFI-40-P	0.1340	0.016	0.0121
MFI-40-4h-2-c1	0.0464	-	0.0039
MFI-40-4h-2-c2	-	-	-
MFI-40-4h-2-c3	0.0625	-	0.0053
MFI-C666	0.3490	0.031	0.0270
MFI-C868	0.6970	0.051	0.0539

[a]Measured rate constants (per total Al) reflect an average or single rate measurement during mesitylene benzylation with DBE (363 K) in the zero-order kinetic regime. Uncertainties range from ±15% to ±30%.
[b]Determined from DTBP desorbed during TPD following DTBP adsorption and flushing. Uncertainties are ±15%.
[c]Estimated using the predicted H^+_{ext} content from measured mesitylene benzylation rate constants (per total Al; Table 1, Main text) and the total Al content (per g zeolite; Table S1, SI). Uncertainties range from ±25% to ±40%.
"-" indicates not measured.

Representative mesitylene benzylation reaction profiles are shown for each sample studied in Figures S17 to S27.

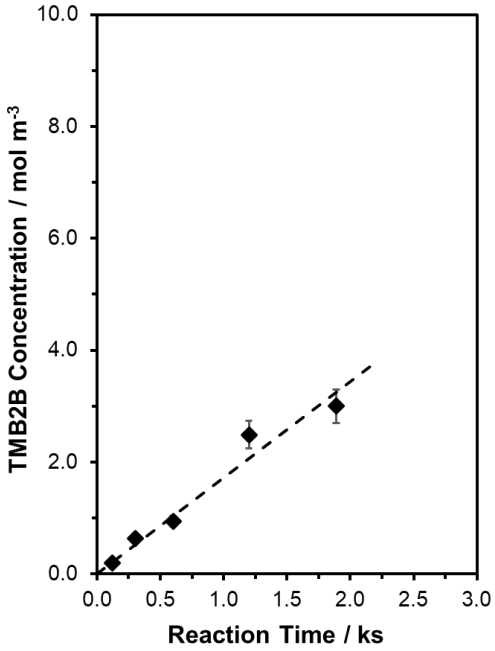

Figure S17. Concentrations of TMB2B as a function of batch reaction time during mesitylene benzylation (363 K) with DBE as a function of batch reaction time on MFI-C868. Conditions: TMB concentration: 6700 mol m^{-3}; DBE concentration = 400 mol m^{-3}; Volume of solution: 5.4 cm^3; Catalyst mass: 0.039 g.

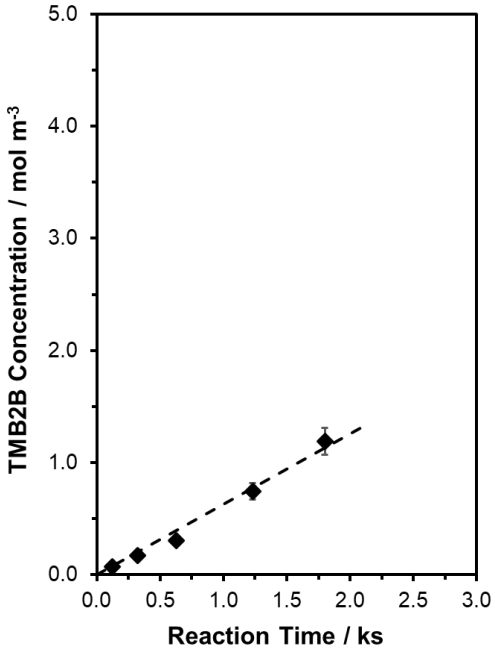

Figure S18. Concentrations of TMB2B as a function of batch reaction time during mesitylene benzylation (363 K) with DBE as a function of batch reaction time on MFI-C666. Conditions: TMB concentration: 6700 mol m^{-3}; DBE concentration = 400 mol m^{-3}; Volume of solution: 5.4 cm^3; Catalyst mass: 0.028 g.

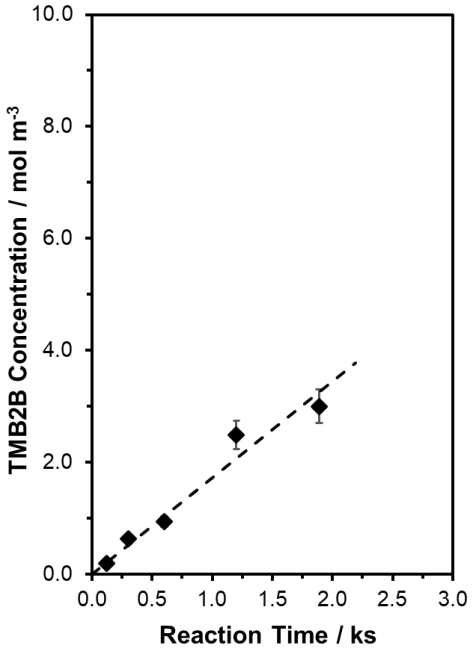

Figure S19. Concentrations of TMB2B as a function of batch reaction time during mesitylene benzylation (363 K) with DBE as a function of batch reaction time on MFI-13-P. Conditions: TMB concentration: 6900 mol m^{-3}; DBE concentration = 200 mol m^{-3}; Volume of solution: 5.2 cm^3; Catalyst mass: 0.051 g.

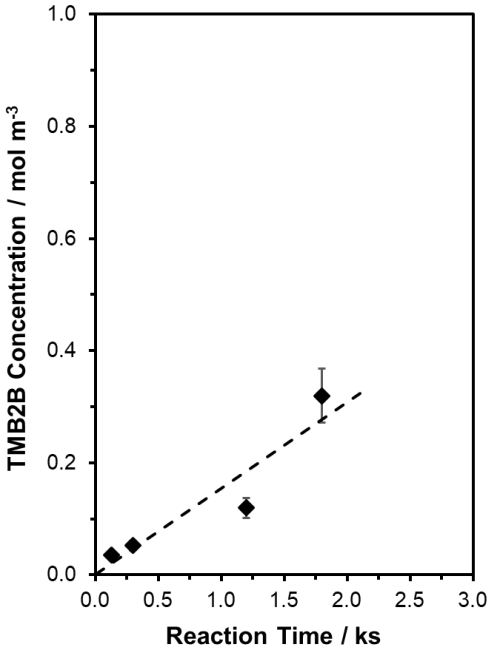

Figure S20. Concentrations of TMB2B as a function of batch reaction time during mesitylene benzylation (363 K) with DBE as a function of batch reaction time on MFI-13-4h-2-c1. Conditions: TMB concentration: 6700 mol m^{-3}; DBE concentration = 400 mol m^{-3}; Volume of solution: 5.4 cm^3; Catalyst mass: 0.050 g.

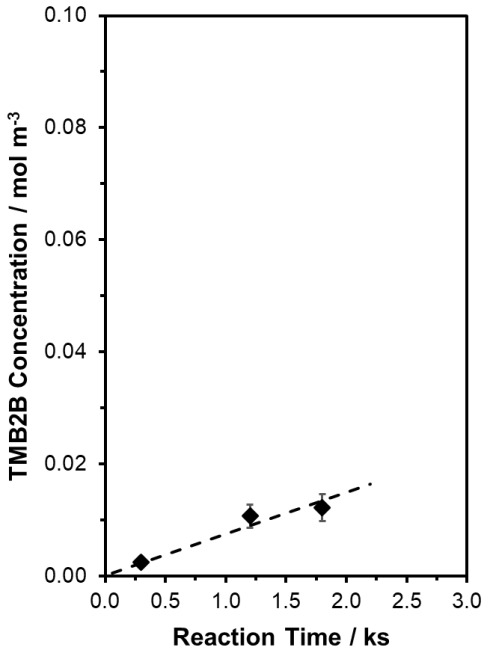

Figure S21. Concentrations of TMB2B as a function of batch reaction time during mesitylene benzylation (363 K) with DBE as a function of batch reaction time on MFI-13-4h-2-c2. Conditions: TMB concentration: 6700 mol m^{-3}; DBE concentration = 400 mol m^{-3}; Volume of solution: 5.4 cm^3; Catalyst mass: 0.052 g.

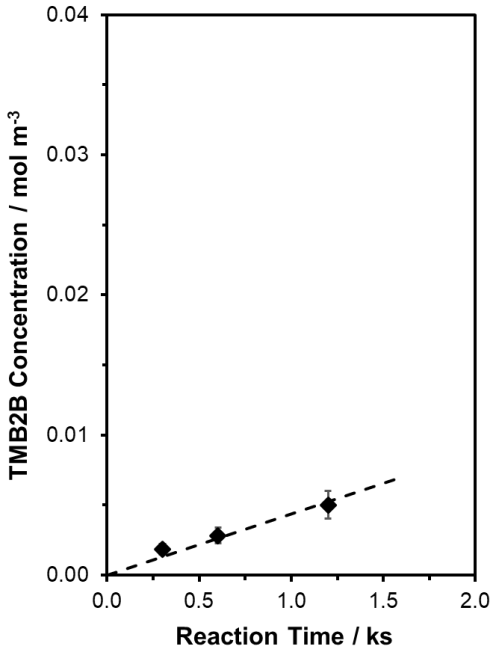

Figure S22. Concentrations of TMB2B as a function of batch reaction time during mesitylene benzylation (363 K) with DBE as a function of batch reaction time on MFI-13-4h-2-c3. Conditions: TMB concentration: 6700 mol m^{-3}; DBE concentration = 400 mol m^{-3}; Volume of solution: 5.4 cm^3; Catalyst mass: 0.050 g.

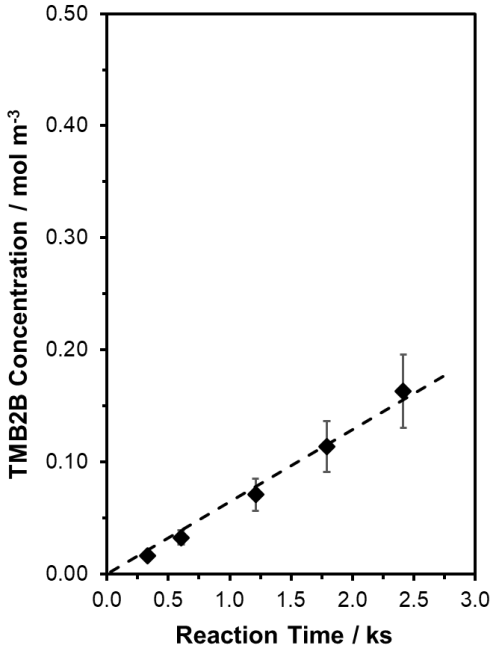

Figure S23. Concentrations of TMB2B as a function of batch reaction time during mesitylene benzylation (363 K) with DBE as a function of batch reaction time on MFI-16-P. Conditions: TMB concentration: 6700 mol m^{-3}; DBE concentration = 400 mol m^{-3}; Volume of solution: 5.4 cm^3; Catalyst mass: 0.051 g.

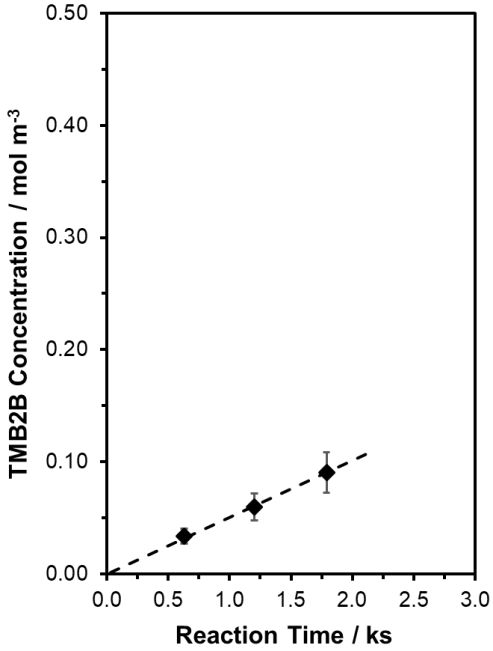

Figure S24. Concentrations of TMB2B as a function of batch reaction time during mesitylene benzylation (363 K) with DBE as a function of batch reaction time on MFI-16-4h-2-c1. Conditions: TMB concentration: 6700 mol m^{-3}; DBE concentration = 400 mol m^{-3}; Volume of solution: 5.4 cm^3; Catalyst mass: 0.100 g.

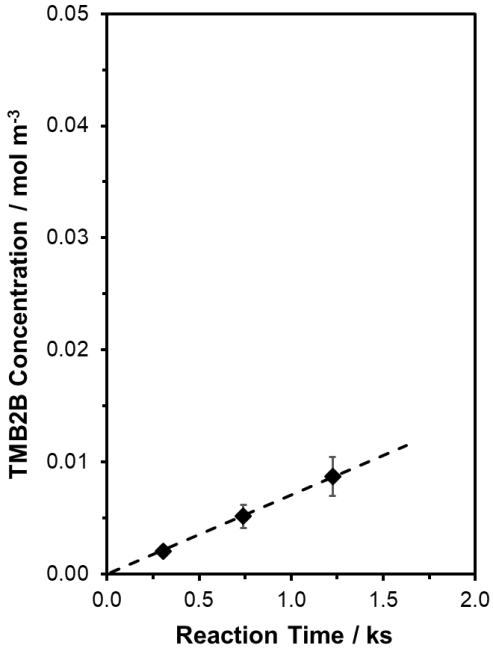

Figure S25. Concentrations of TMB2B as a function of batch reaction time during mesitylene benzylation (363 K) with DBE as a function of batch reaction time on MFI-16-4h-2-c3. Conditions: TMB concentration: 6700 mol m^{-3}; DBE concentration = 400 mol m^{-3}; Volume of solution: 5.4 cm^3; Catalyst mass: 0.052 g.

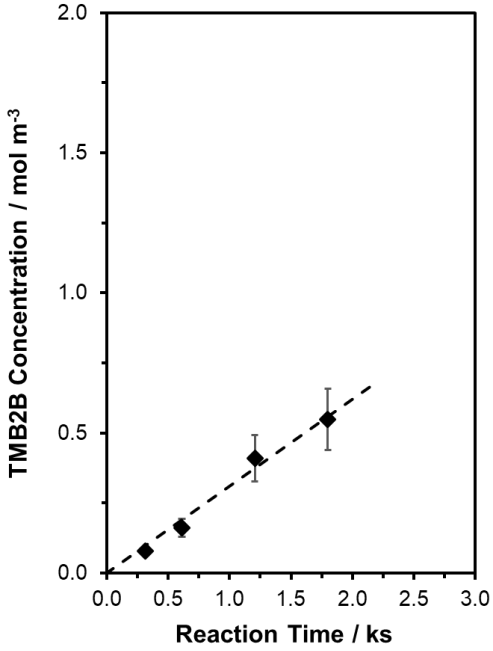

Figure S26. Concentrations of TMB2B as a function of batch reaction time during mesitylene benzylation (363 K) with DBE as a function of batch reaction time on MFI-40-4h-2-c1. Conditions: TMB concentration: 6700 mol m^{-3}; DBE concentration = 400 mol m^{-3}; Volume of solution: 5.4 cm^3; Catalyst mass: 0.091 g.

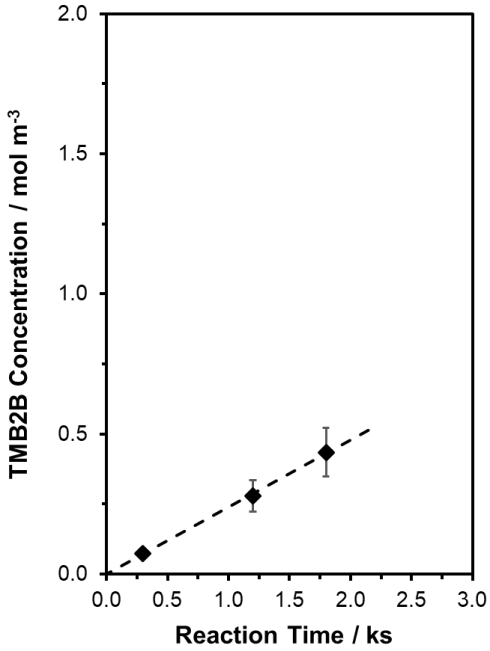

Figure S27. Concentrations of TMB2B as a function of batch reaction time during mesitylene benzylation (363 K) with DBE as a function of batch reaction time on MFI-40-4h-2-c3. Conditions: TMB concentration: 6700 mol m^{-3}; DBE concentration = 400 mol m^{-3}; Volume of solution: 5.4 cm^3; Catalyst mass: 0.051 g.

References

1 C. Freitas, N. S. Barrow and V. Zholobenko, *Johns. Matthey Technol. Rev.*, 2018, **62**, 279–290.
2 D. Yi, X. Xu, X. Meng, N. Liu and L. Shi, *J. Porous Mater.*, 2019, **26**, 1767–1779.
3 K. Góra-Marek, K. Tarach and M. Choi, *J. Phys. Chem. C*, 2014, **118**, 12266–12274.
4 A. Corma, V. Fornés, L. Forni, F. Márquez, J. Martínez-Triguero and D. Moscotti, *J. Catal.*, 1998, **179**, 451–458.
5 J. H. Ahn, R. Kolvenbach, C. Neudeck, S. S. Al-Khattaf, A. Jentys and J. A. Lercher, *J. Catal.*, 2014, **311**, 271–280.
6 A. G. Popov, V. S. Pavlov and I. I. Ivanova, *J. Catal.*, 2016, **335**, 155–164.
7 S. M. T. Almutairi, B. Mezari, E. A. Pidko, P. C. M. M. Magusin and E. J. M. Hensen, *J. Catal.*, 2013, **307**, 194–203.
8 Q. Zhao, W.-H. Chen, S.-J. Huang, Y.-C. Wu, H.-K. Lee and S.-B. Liu, *J. Phys. Chem. B*, 2002, **106**, 4462–4469.
9 Y. Seo, K. Cho, Y. Jung and R. Ryoo, *ACS Catal.*, 2013, **3**, 713–720.
10 S. Zheng, H. R. Heydenrych, A. Jentys and J. A. Lercher, *J. Phys. Chem. B*, 2002, **106**, 9552–9558.
11 M. Li, Y. Hu, Y. Fang and T. Tan, *Catal. Today*, 2020, **339**, 312–320.
12 W. S. Borghard, E. W. Sheppard and H. J. Schoennagel, *Rev. Sci. Instrum.*, 1991, **62**, 2801–2809.
13 M. Thommes, K. Kaneko, A. V. Neimark, J. P. Olivier, F. Rodriguez-Reinoso, J. Rouquerol and K. S. W. Sing, *Pure Appl. Chem.*, 2015, **87**, 1051–1069.
14 N. Fairley, V. Fernandez, M. Richard-Plouet, C. Guillot-Deudon, J. Walton, E. Smith, D. Flahaut, M. Greiner, M. Biesinger, S. Tougaard, D. Morgan and J. Baltrusaitis, *Appl. Surf. Sci. Adv.*, 2021, **5**, 100112.
15 A. E. Hughes, K. G. Wilshier, B. A. Sexton and P. Smart, *J. Catal.*, 1983, **80**, 221–227.
16 J. H. Scofield, *J. Electron Spectrosc. Relat. Phenom.*, 1976, **8**, 129–137.
17 J.-Fr. Tempere, D. Delafosse and J. P. Contour, *Chem. Phys. Lett.*, 1975, **33**, 95–98.
18 S. Svelle, M. Visur, U. Olsbye, Saepurahman and M. Bjørgen, *Top. Catal.*, 2011, **54**, 897.
19 K. De Wispelaere, J. S. Martínez-Espín, M. J. Hoffmann, S. Svelle, U. Olsbye and T. Bligaard, *Catal. Today*, 2018, **312**, 35–43.
20 M. DeLuca, P. Kravchenko, A. Hoffman and D. Hibbitts, *ACS Catal.*, 2019, **9**, 6444–6460.
21 M. Bocus, L. Vanduyfhuys, F. De Proft, B. M. Weckhuysen and V. Van Speybroeck, *JACS Au*, 2022, **2**, 502–514.
22 D. Acharya, W. Chen, J. Yuan, Z. Liu, X. Yi, Y. Xiao and A. Zheng, *Catal. Lett.*, 2021, **151**, 3048–3056.
23 S. Xing, K. Liu, T. Wang, R. Zhang and M. Han, *Catal. Sci. Technol.*, 2021, **11**, 2792–2804.
24 T. W. G. Solomons, C. B. Fryhle and S. A. Snyder, *Organic Chemistry, 12th Edition*, Wiley Global Education, 2016.
25 H. Eyring, *J. Chem. Phys.*, 1935, **3**, 107–115.
26 M. G. Evans and M. Polanyi, *Trans. Faraday Soc.*, 1935, **31**, 875–894.
27 R. Gounder and E. Iglesia, *Chem. Commun.*, 2013, **49**, 3491–3509.
28 H. I. Adawi, F. O. Odigie and M. L. Sarazen, *Mol. Syst. Des. Eng.*, 2021, **6**, 903–917.
29 M. DeLuca and D. Hibbitts, *Microporous Mesoporous Mater.*, 2022, **333**, 111705.
30 A. J. Jones and E. Iglesia, *ACS Catal.*, 2015, **5**, 5741–5755.

31 H. Balcom, A. J. Hoffman, H. Locht and D. Hibbitts, *ACS Catal.*, 2023, **13**, 4470–4487.
32 X. Zhang, D. Liu, D. Xu, S. Asahina, K. A. Cychosz, K. V. Agrawal, Y. A. Wahedi, A. Bhan, S. A. Hashimi, O. Terasaki, M. Thommes and M. Tsapatsis, *Science*, 2012, **336**, 1684–1687.
33 C. Li, H. J. Cho, Z. Wang, J. Gou, Y. Ren, H. Xi and W. Fan, *ChemCatChem*, 2016, **8**, 2406–2414.
34 D. Liu, X. Zhang, A. Bhan and M. Tsapatsis, *Microporous Mesoporous Mater.*, 2014, **200**, 287–290.
35 R. J. Davis, in *Catalysis for the Conversion of Biomass and Its Derivatives*, Max-Planck-Gesellschaft zur Förderung der Wissenschaften, Berlin, 2013.
36 D. Xu, O. Abdelrahman, S. H. Ahn, Y. Guefrachi, A. Kuznetsov, L. Ren, S. Hwang, M. Khaleel, S. Al Hassan, D. Liu, S. B. Hong, P. Dauenhauer and M. Tsapatsis, *AIChE J.*, 2019, **65**, 1067–1075.
37 R. M. Koros and E. J. Nowak, *Chem. Eng. Sci.*, 1967, **22**, 470.
38 R. J. Madon and M. Boudart, *Ind. Eng. Chem. Fundam.*, 1982, **21**, 438–447.